Proceedings of ASME Turbo Expo 2011
GT2011
June 6-10, 2011, Vancouver, British Columbia, Canada

GT2011-45763

ON THE NONLINEAR DYNAMICS OF ROTOR-FOIL BEARING SYSTEMS: EFFECTS OF SHAFT ACCELERATION, MASS IMBALANCE AND BEARING MECHANICAL ENERGY DISSIPATION

Luis San Andrés
Mast-Childs Professor, Fellow ASME

Keun Ryu
Research Assistant

Mechanical Engineering Dept., Texas A&M University
College Station, TX 77843

ABSTRACT

Gas foil bearing (GFB) technology has reached great maturity as per engineered design and construction and its system integration into rotating machinery. Empirical research has gone beyond showing a few instances of acceptable mechanical performance, to demonstrate GFB multiple-cycle repeatable performance in spite of persistent large amplitude sub synchronous whirl motions. A GFB is a forgiving mechanical element whose engineered resilient underspring structure contains and ameliorates large rotor excursions. Analyses, however, fail to distinguish the hardening stiffness from the FB underspring structure, which under conditions of large force excitations due to imbalance, produces a complex rotordynamic behavior, rich in sub harmonic motions when operating at super critical speeds. This paper extends an earlier analysis of a rigid rotor-GFB system that dispenses with the gas film component to predict the effect of shaft rotation acceleration/deceleration on rotor amplitudes of motion and whirl frequency content. For operation above the system critical speed and as the rotor accelerates, large amplitude whirl motions appear with a main subsynchronous frequency tracking rotor speed, first at 50% speed and later bifurcating into at 33% whirl frequency. Rotor imbalance awakens and exacerbates the system nonlinear response. Slow rotor accelerations result in responses with more abundant subsynchronous whirl patterns, increased amplitudes of whirl, and accompanied by a pronounced mechanical hysteresis when the rotor decelerates. Large rotor imbalances produce both jump phenomenon and a stronger hysteresis during slow acceleration and deceleration cases. Material damping (dry friction) in the FB aids to reduce and delay the nonlinear response, eventually eliminating the multiple frequency behavior. The results bring to attention rotordynamic issues during start up and shut down events that can result from an inadequate FB technology or an unacceptable rotor imbalance grade condition.

INTRODUCTION

Gas foil bearings (GFBs) are widely employed in oil-free microturbomachinery (MTM) such as air cycle machines and micro gas turbines, due to their distinctive advantages over rolling element bearings. Elimination of the oil lubrication system in MTM significantly reduces overall system weight, complexity, and maintenance cost. GFBs also increase system efficiency due to their low power losses and extended maintenance intervals [1,2].

Research at the authors' laboratory has developed GFB computational tools, see Refs. [3-5], benchmarked against reliable test data [6-10]. The models account for most relevant physical aspects and predict foil bearing static and dynamic linear forced performance, power loss, and the management of thermal energy in high temperature environments. While performing the experimental work, it became evident (to the authors) that GFBs are highly nonlinear mechanical elements that produce complicated RBS motions when operating at high speeds, i.e., above the RBS critical speed. Incidentally, there is abundant experimental and field data demonstrating the complex rotordynamic behavior of rotor-GFB systems; namely, rotor motions of large amplitude and sub synchronous in character [7-9]. Although well documented, the phenomenon is still misunderstood; see for example test data and discussion in Refs. [11,12].

The appearance of the sub synchronous whirl motions is not a self-excited phenomenon, i.e., typical instability. In operation, increasing rotor imbalance (a forcing function) further aggravates the persistence and severity of the sub harmonic whirl motions [7-9]. Most importantly, however, the forgiving nature of a GFB does not produce sudden failure of the RBS in spite of the exceedingly large orbital motions. The resilience of the underspring structure explains the remarkable behavior.

Figure 1 [9] displays typical rotor motions recorded on a test rig with a solid (1 kg) rotor supported on 2nd generation GFBs. While the rotor coasts down from a high speed (50 krpm) to rest, there is dominance of sub harmonic motions, mainly locked at the system natural frequency (140-180 Hz) that persists from the top speed to a rotor speed at about thee times the natural frequency (27 krpm [450 Hz]). The RBS motion is a forced nonlinear phenomenon due to the hardening nonlinearity of the FB elastic structure. Internal resonances at rotor speeds

equal to twice and thrice the system natural frequency are particularly important. For the data shown in Fig. 1, the rotor condition was close to perfectly balanced while the support foil bearings offered little damping; hence the extreme sensitivity of the system to excite its natural frequency over extended regions of the operating speed range.

References [8,9] present further measured RBS motions with rich sub harmonic content and introduce mechanical changes and air supply conditions aiding to delay the onset and amplitude severity of the sub harmonic whirl motions.

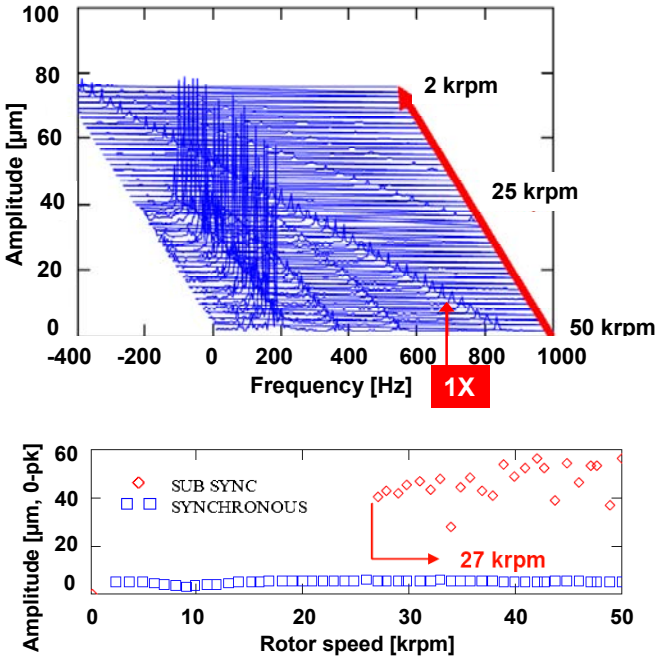

Fig. 1 Test data from rotor supported on 2nd generation GFBs. Top: Waterfall of rotor motion while decelerating from 50 krpm. Bottom: Amplitudes of rotor motion (synchronous and subsynchronous) versus rotor speed. Taken from Ref. [9]

This paper extends an earlier analysis [13] to predict the forced response of a rigid rotor supported on FBs modeled as nonlinear third order structural elements with material damping. Reference [13] reviews the past literature showcasing experimental evidence of nonlinear behavior in rotor-GFB systems. The simple FB model assumes a minute gas film with an *infinite* stiffness. Hence, the FB reaction force is eminently of structural type. Predictions from the analysis agree with RBS laboratory measurements in Ref. [7]. The numerical results evidence a Duffing-like dynamic behavior with multiple frequency responses, sub- and super-harmonic, within certain ranges of rotor speed [14-16]. Incidentally, recent Refs. [17,18] reporting measurements of GFB forced motions and the identification of force coefficients call to attention to the strong nonlinearities apparent in GFBs.

In the early analysis [13], the rotor speed is held constant. The predictions thus represent (quasi) steady-state conditions at a particular rotor speed. Presently, the analysis seeks to determine the effect of rotor acceleration (speed ramp rate), imbalance mass magnitude, and the FB structural loss factor – a measure of the bearing mechanical energy dissipation- on the dynamic response of a simple RBS. Note that fast accelerations are typical in small size rotating machinery since the rotor mass moments of inertia are small. In automotive turbochargers, for example, shaft accelerations (or decelerations) at rates as large as 1 kHz/s (60 krpm/s) are not uncommon [19].

SIMPLE STRUCTURAL MODEL FOR FOIL BEARING

For a 2nd generation FB, Fig. 2 depicts the recorded bearing radial deflection for a range of static loads [13]. The measurements show a highly nonlinear structural behavior with distinctive paths during the loading and unloading processes, thus evidencing mechanical hysteresis. The hardening stiffness is likely to induce internal resonances [20] at rotor speeds greater than the RBS natural frequency [6].

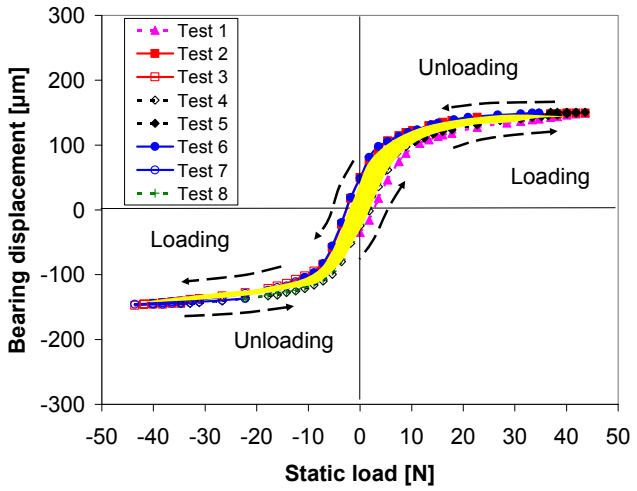

Fig. 2 Measured FB displacement versus static load during eight load and unload tests. Taken from Ref. [13]

The FB structural reaction force (F_{FB_s}) is best represented as a third order polynomial in the radial displacement (r), i.e.

$$F_{FB_s} = K_1 r + K_2 r^2 + K_3 r^3 \qquad (1)$$

where $K_1 = 6.75\,10^4 \frac{N}{m}$, $K_2 = -2\,10^9 \frac{N}{m^2}$, $K_3 = 10^{14} \frac{N}{m^3}$ as given in Ref. [13]. Figure 3 depicts Eq. (1) to demonstrate the nonlinear behavior of the FB as well as the local (nonlinear) stiffness, $K_{FB_s} = \partial K_{FB_s} / \partial r$. Note that neither the FB reaction force nor its local structural stiffness is symmetric about the null load condition. The behavior is typical and depends on the orientation of the applied load relative to the angular location of the spot weld affixing the top and bottom foils to the bearing cartridge [21,22].

From the load versus deflection hysteresis loop in Fig. 2, a structural damping with loss factor (γ) = 0.14 represents best the FB mechanical energy dissipation mechanism [13]. A similar loss factor magnitude is obtained from shaker induced dynamic loads on the same FB [21,22].

Prior art [7-9] describes the test rig comprising of a solid rotor supported on a pair of 2nd generation GFBs. Measurements, supported by rotordynamic analyses, demonstrate the test rotor, weighing 10 N, behaves as a rigid

body for shaft speeds below 50 krpm (833.3 Hz) [7]. Note that the test rotor center of gravity is nearly equidistant from the two supporting bearings. Hence, for in-phase imbalance conditions, the rotor is regarded as a point mass (M=1.02 kg). Figure 4 shows a schematic view of the model point mass rotor on its FBs and the coordinate system for analysis.

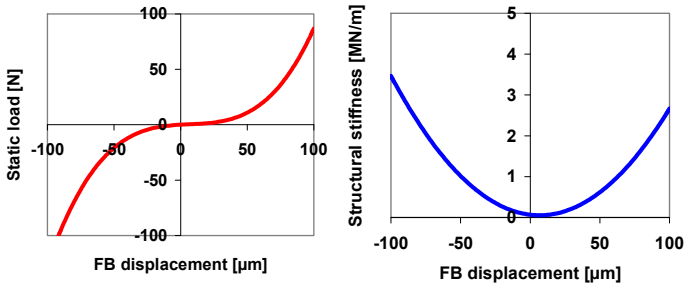

Fig. 3 Typical foil bearing structural force (F_{FBs}) and stiffness (K_{FBs}) versus radial deflection (r)

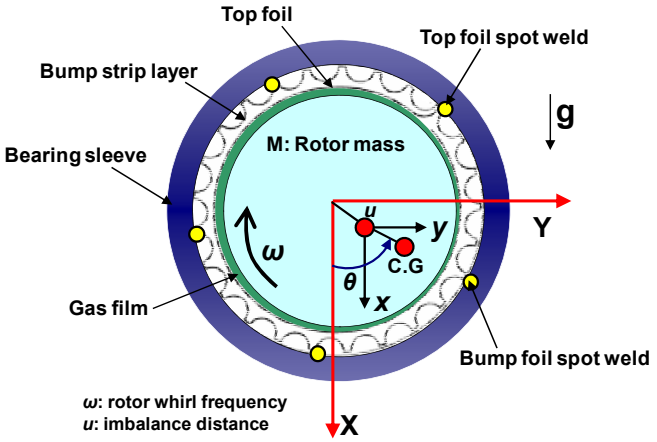

Fig. 4 Schematic view of rigid rotor supported on foil bearing and its coordinate system

Let (x,y) denote the vertical and horizontal displacements of the rotor mass center, and u as the mass imbalance offset. The equations of motion for the RBS are

$$\begin{aligned} M\ddot{x} + 2F_{FB_x} &= Mu\left[\Omega^2\cos(\theta) + \alpha\sin(\theta)\right] + Mg \\ M\ddot{y} + 2F_{FB_y} &= Mu\left[\Omega^2\sin(\theta) - \alpha\cos(\theta)\right] \end{aligned} \tag{2}$$

where the rotor angular speed (Ω) and angular displacement (θ) are defined in terms of a constant[1] acceleration (α)

$$\Omega = \int_0^t \alpha\, dt = \alpha t + \Omega_i\,;\quad \theta = \int_0^t \Omega\, dt = \tfrac{1}{2}\alpha t^2 + \Omega_i t \tag{3}$$

The vertical and horizontal components of the FB dynamic reaction force are [13]

$$F_{FB_x} = \frac{F_{FB_s}}{r}\left(x + \frac{\gamma}{\Omega}\dot{x}\right);\quad F_{FB_y} = \frac{F_{FB_s}}{r}\left(y + \frac{\gamma}{\Omega}\dot{y}\right); \tag{4}$$

[1] The selected constant accelerations is a matter of convenience. Other time variations can be readily implemented in the computational model.

with $r = \sqrt{(x^2 + y^2)}$. In actual operation and whence the rotor is airborne, a gas film separates the rotor from the top foil. Presently, this gas film is regarded as minute and hence of infinite stiffness. This is the fundamental assumption of the model hereby implemented. Note that the model in Eq. (4) is strictly valid for a structure with linear stiffness; the nonlinear extension follows simplicity and its ability to reproduce recorded measurements, see Ref. [13].

The static equilibrium solution of Eq. (2), i.e. with u=0, gives the nonlinear relationship

$$x_E\left(K_1 + K_2\, x_E + K_3\, x_E^2\right) = \frac{M\, g}{2};\quad y_E = 0 \tag{5}$$

and the RBS natural frequency (f_n) for small amplitude motions about the equilibrium condition (x_E, y_E) is

$$f_n = \frac{1}{2\pi}\sqrt{\frac{2\,K_{FB_s}(x_E)}{M}} = \frac{1}{2\pi}\sqrt{\frac{2\left(K_1 + 2\,K_2\, x_E + 3K_3\, x_E^2\right)}{M}} \tag{6}$$

Presently, x_E=37.5 μm and f_n=130 Hz (7,797 rpm).

The homogeneous form of Eq. (1) with K_2=0 reproduces a Duffing-like oscillator [15] with hysteretic damping. For the undamped case (γ=0), a harmonic balance analysis predicts operating speed regions with multiple frequencies; in particular sub harmonic (⅓ frequency) responses occur for rotor speeds higher than three times the system natural frequency (f_n). Larger imbalance displacements (u), i.e., a forced excitation, tend to exacerbate the whirl amplitudes of motion [13].

Eqs. (2) and (3) are written in state-space form for ready numerical integration using a fourth-order Runge-Kutta scheme available in a mathematical software package. In the examples that follow, the rotor speed increases from Ω_i=2 krpm (209 rad/s) to Ω_T = 36 krpm (3,770 rad/s), or decreases from Ω_i=36 krpm to Ω_T = 2 krpm. The rotor acceleration α is constant to reproduce slow, moderate, and fast shaft speed ramp rates lasting 16 s (α=±35 Hz/s), 8 s (α=±71 Hz/s), and 2 s (α=±283 Hz/s), respectively.

In the numerical integration, the sampling rates for the fast, moderate and slow rotor ramp rates are 96k/s, 24k/s, and 12k/s, respectively; with corresponding time steps (Δt) = 0.01042 ms, 0.04167 ms, and 0.0833 ms. The fast rotor acceleration requires of a smaller time step (faster acquisition rate) since the speed changes quickly. In all the cases, the total number of integration points (samples) is 192,000. In the integration procedure, spanning an integer number of rotor revolutions, the initial conditions for rotor acceleration cases are x=x_E, y=0, $\dot{x} = \dot{y} = 0$, θ=0, Ω=Ω_i. The last state during rotor acceleration is used as the initial condition for the cases with rotor deceleration from Ω_T = 36 krpm. For example, the initial conditions for α=-283.3 Hz/s are x=-42 μm, y=98 μm, $\dot{x}$ = 7.8 mm/s, $\dot{y}$ = 15.5 mm/s, θ=3979 rad, and Ω_i=3770 rad/s. The CPU execution time to complete the analysis is just a few seconds in a PC.

At u=8 μm and γ=0.14, Fig. 5 depicts the predicted rotor vertical motions (x) versus rotor speed during the fast rotor speed ramp rate at ± 283 Hz/s. The top graph shows x as the rotor accelerates, and since the acceleration (α+) is constant, the horizontal scale is tantamount to increasing time (2s overall). The bottom graph shows rotor displacements during

deceleration (α<0) from a top sped of 36 krpm (600 Hz). The graphs show vertical lines labeling the RBS (linear model) natural frequency ($1\times f_n$) and twice and thrice its magnitude ($2\times f_n$ and $3\times f_n$). The dense graphs (192 k points!) show complicated rotor motions with operating speed regions where bursts of large amplitude displacements are apparent. Little knowledge is gained from these graphs, except to realize that the motions when the rotor accelerates or decelerates are different.

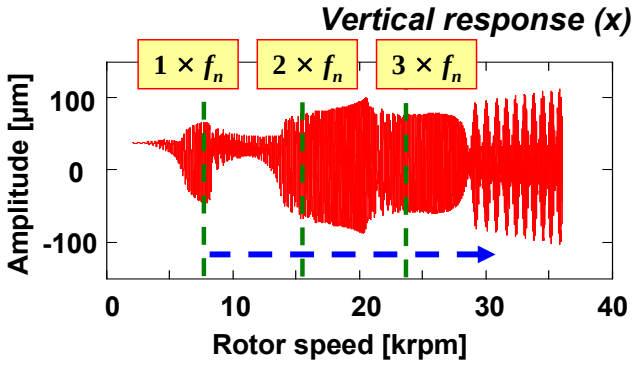

(a) Rotor acceleration +283 Hz/s

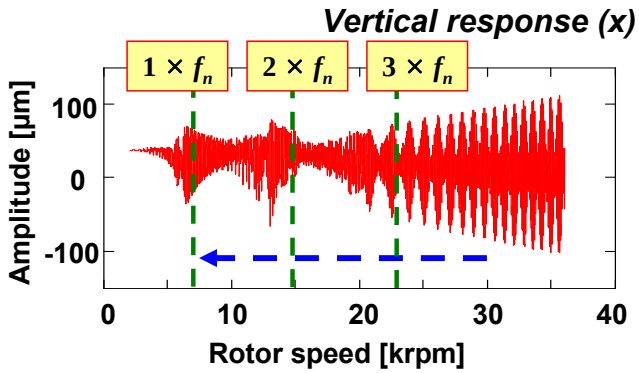

(b) Rotor deceleration -283 Hz/s

Fig. 5 Predicted rotor time response in vertical direction (*x*). Speed ramp rate ± 283 Hz/s. Imbalance *u*=8 µm. FB *γ*=0.14

Post processing of the numerical responses in the frequency domain produces waterfalls of rotor motion displacements; and by using digital filters, delivers the amplitude of synchronous response, as well as any other amplitudes associated to either sub or super harmonic frequencies, if existent. Figure 6 depicts the predicted waterfall of vertical (x) rotor motions as the rotor speed increases to 36 krpm (top graph) and then decelerates to 2 krpm (bottom graph). Note the synchronous response (1X) and the richness of sub harmonic whirl motions with large amplitudes. These whirl motions are most severe as the rotor accelerates[2] towards its top speed (36 krpm).

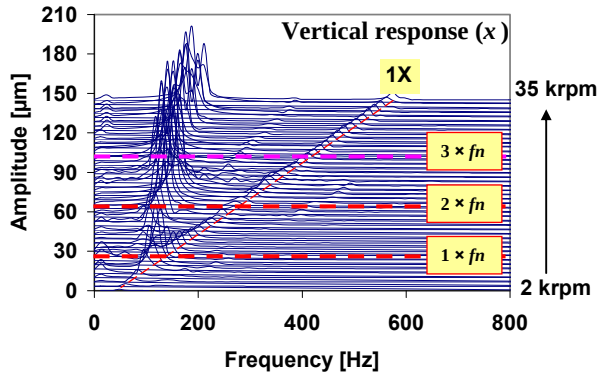

(a) Acceleration +283 Hz/s

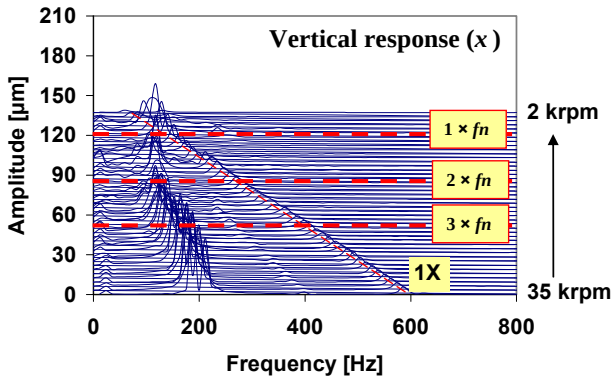

(b) Deceleration -283 Hz/s

Fig. 6 Waterfalls of rotor vertical (*x*) motion as rotor (a) accelerates and (b) decelerates. Rotor speed ramp rate ±283 Hz/s. Imbalance *u*=8 µm. FB *γ*=0.14.

RBS RESPONSE PREDICTIONS AND DISCUSSION

Effect of rotor acceleration on RBS response

Below, the whirl frequency ratio (WFR=ω/Ω) relates the sub synchronous whirl frequency (ω) to the rotor angular frequency (Ω). During rotor acceleration, low to fast speed ramp rates, Fig. 7 shows the contour plot of vertical rotor motions (x), the WFR, and amplitudes of motion at synchronous speed (1X) and subsynchronous frequencies (~½WFR and ~⅓ WFR)[3] versus rotor speed. In the contour plots showcasing the frequency content of rotor motions, bright to dull colors denote large to small amplitudes of motion, respectively. The imbalance displacement and the FB structural loss factor (γ) are 8 µm and 0.14, respectively.

Predicted motions along the horizontal direction (y) are not shown for brevity. The y-displacements are also rich in subsynchronous components as in the vertical (x) motions; albeit there are differences on the frequency ranges over which the ½WFR motions are apparent, for example.

At rotor speeds lower than and just above the system natural frequency (f_n =130 Hz), no sub synchronous motions are apparent. However, for rotor speeds above 10 krpm (167 Hz), there is an abundance of large amplitude sub harmonic motions. Subsynchronous whirl motions appear from 11 to 20 krpm with WFR=½ at first, and later from 20 to 36 krpm jump to

[2] This assertion is not general since a highly nonlinear response depends on the system initial state.

[3] WFRs=0.45 to 0.55 and WFRs=0.28 to 0.38 are combined to represent ~½WFR and ~⅓WFR, respectively

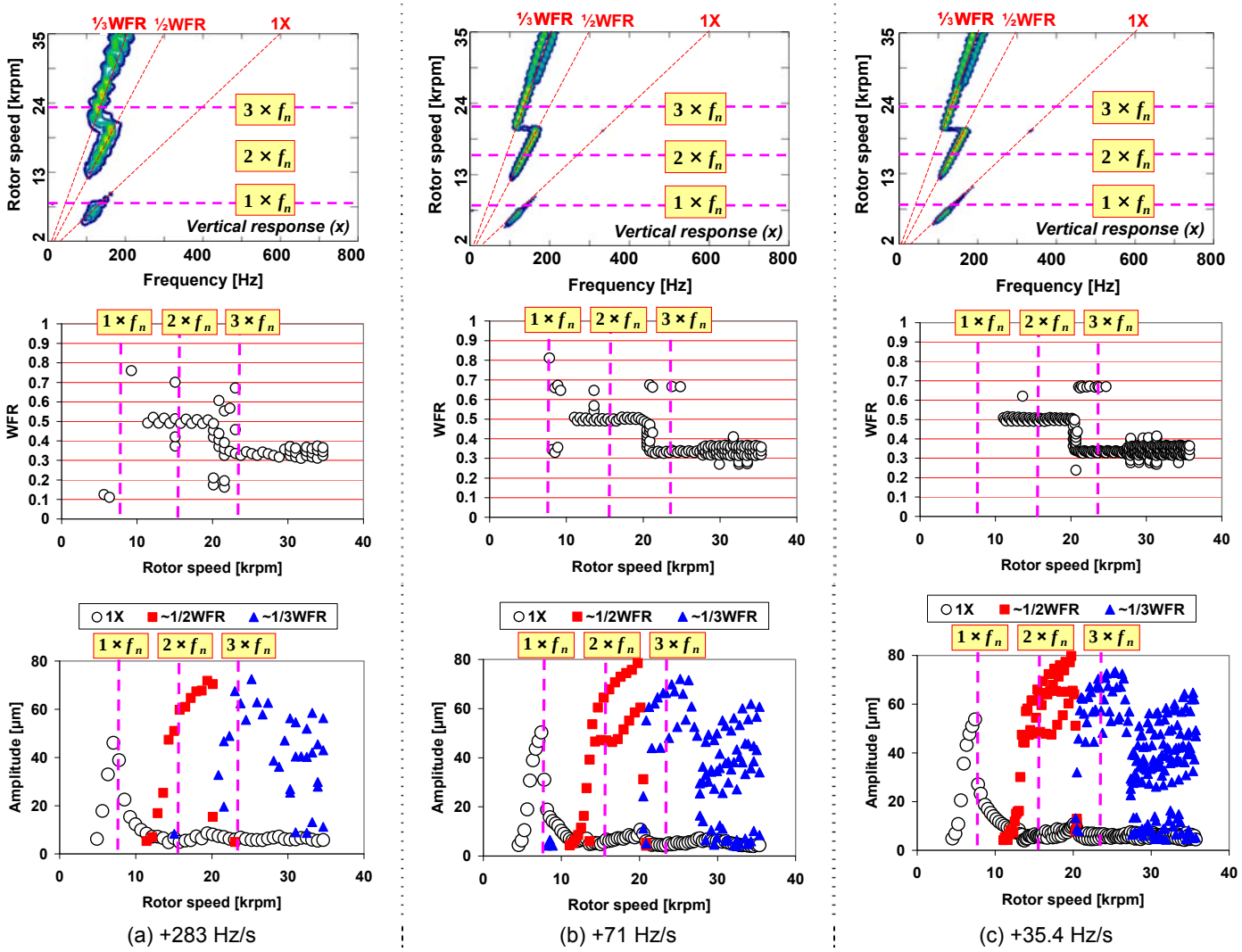

Fig. 7 Predicted rotor vertical (*x*) motion amplitudes while rotor accelerates. *α*= +283 Hz/s, +71 Hz/s and +35.4 Hz/s (left to right graphs). (Top) vibration contour plots, (Middle) whirl frequency ratio, and (Bottom) amplitudes of synchronous and subsynchronous (~½WFR and ~⅓WFR) motions versus rotor speed. Imbalance *u*=8 μm and FB: *γ*=0.14

WFR=⅓. For rotor speeds above 28 krpm, the whirl motions show more complex WFRs ranging from 0.31 to 0.37, slightly above and below ⅓. Once a subsynchronous frequency motion appears, its amplitude rapidly increases with rotor speed. Note that significant motion amplitudes with whirl frequencies at 50% and 33% of angular frequency (Ω) appear for operation at rotor speeds just above ~twice and ~three times the system natural frequency, i.e. the internal resonances of the nonlinear RBS. The sub harmonic motions are not locked at the system natural frequency but track the rotor angular speed at either ½ Ω or ⅓ Ω whirl frequency.

As the rotor speed ramp rate increases, the peak amplitude of synchronous response (bottom graphs in Fig. 7) increases slightly while traversing the system critical speed (46 μm for 283 Hz/s, 50 μm for 71 Hz/s, and 54 μm for 35.4 Hz/s). At ~20 krpm (333 Hz), the rotor whirl motions jump from ω=½Ω to ω=⅓ Ω. The subsynchronous vibrations are more severe for the slower speed ramp rate (rightmost graphs) since there is more elapsed time for the whirl motions to build up. Incidentally, the highest rotor acceleration renders a broad frequency spectrum around ~⅓WFR with a less marked transition at the jump frequency. The frequency jump phenomenon is well documented in automotive turbochargers supported on (semi) floating ring bearings, see Ref. [19].

During rotor deceleration, Fig. 8 shows similar graphs filtering the rotor motion into its synchronous and major sub synchronous whirl components. Note that the peak amplitudes of synchronous whirl (1X) remain similar, irrespective of the shaft deceleration rate. The overall rotor response whirl amplitudes, synchronous and sub, during rotor deceleration are smaller than those while the rotor accelerates. For rotor speeds > ~20 krpm (333 Hz), motions with WFRs ranging from 0.27 to 0.41, i.e. nearly a chaotic regime, are apparent. Note also that the motions with a 50% WFR are not as severe in amplitude as when the rotor accelerates and occur over a shorter rotor speed span; i.e., WFR=½ establishes from Ω= 18.3 krpm→11.2 krpm while decelerating. On the other hand, while accelerating, motions with WFR=½ persist from Ω=11.2 krpm→20.9 krpm. Incidentally, the marked differences in the onset speed and persistence of whirl motions show the RBS has a marked mechanical hysteresis [19,23].

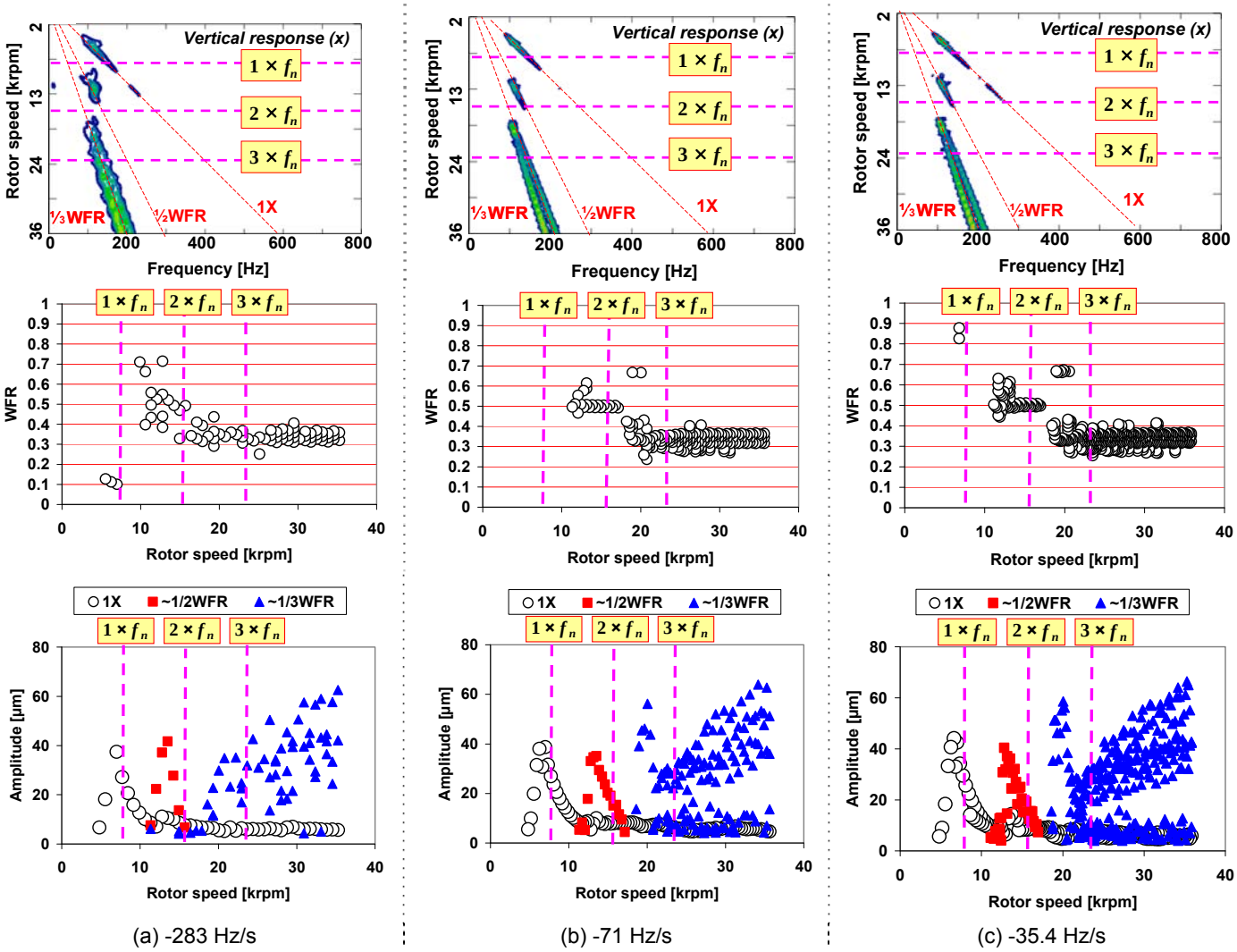

Fig. 8 Predicted rotor vertical (*x*) motion amplitudes while rotor decelerates. *α*=-283 Hz/s, -71 Hz/s and -35.4 Hz/s (left to right graphs). (Top) vibration amplitude contour plots, (Middle) whirl frequency ratio, and (Bottom) amplitudes of synchronous and subsynchronous (~½WFR and ~⅓WFR) motions versus rotor speed. Imbalance *u*=8 μm and FB: *γ*=0.14

For comparison, Fig. 9 depicts the amplitudes of rotor synchronous motion versus shaft speed obtained for the slow rotor acceleration at ±71 Hz/s. The figure also displays the amplitude of the linear RBS response [24], with $f=\Omega/2\pi$ as the frequency of the rotor spinning speed.

$$x_L = u\frac{(r')^2}{\sqrt{\left[1-(r')^2\right]^2+(\gamma r')^2}}\ ;\ \text{with}\ \ r'=\frac{f}{f_n} \qquad (7)$$

The linear rotor response peaks at ~7.8 krpm at a frequency very near the linearized RBS natural frequency (f_n). Operation at this frequency gives[4] $x_L = u/\gamma$ = 8 μm/0.14 = 57.1 μm. There is little discrepancy between the linear RBS response and the synchronous response obtained numerically. Incidentally, note that the peak amplitude during the shaft deceleration is ~10 μm smaller than the one predicted during rotor acceleration. The minor differences noted may suggest the RBS behaves linearly; however, recall the abundant sub harmonic motions found and displayed in Figs. 7 and 8. Reference [25] makes a similar observation albeit for a more complicated RBS.

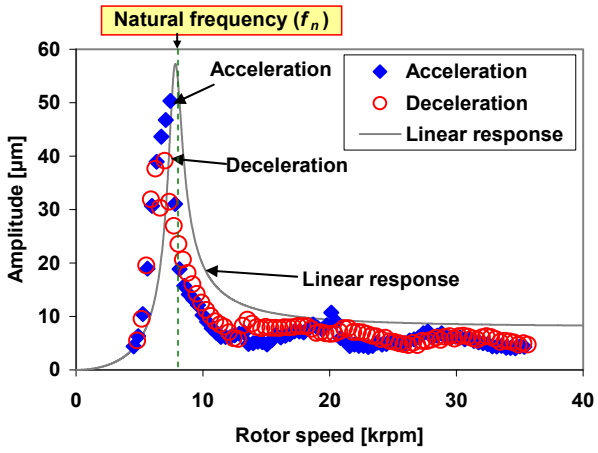

Fig. 9 Amplitudes of rotor synchronous motion during rotor acceleration and deceleration *α*=+/- 71 Hz/s). Response for linear RBS also shown. Imbalance *u*=8 μm, and FB: *γ*=0.14.

[4] In the linearized system, the equivalent viscous damping ratio $\zeta = \gamma/2 = 0.07$ (7%), not an insignificant magnitude.

Effect of rotor mass imbalance on RBS response

During rotor acceleration at α=283 Hz/s, Fig. 10 shows the contour plot of vertical rotor motions (x), the whirl frequency ratio (WFR=ω/Ω), and components of synchronous (1X) and subsynchronous whirl motions (~½WFR and ~⅓WFR) versus rotor speed. The graphs, left to right, correspond to predicted responses for increasing imbalances, u=4, 16 and 20 µm. See Fig. 7 for results with u=8 µm. It is apparent that the imbalance magnitude exacerbates the bearings' nonlinearity and showcases a distinctive jump phenomenon [26]. Most importantly, as the imbalance u increases, and for rotor speeds above ($3\times f_n$), the rotor motion has a broader frequency spectra with whirl motions at mostly ⅓ WFR. The ½ frequency whirl disappears as imbalance increases. Note that other predictions evidence no sub harmonic whirl for u < 4 µm. The imbalance magnitude does affect the rotor speeds at which the sub harmonic motions with 50% and 33% whirl frequencies appear (or disappear).

During rotor deceleration at -283 Hz/s, Fig. 11 depicts the contour plot of vertical (x) rotor motion for the largest imbalance u =20 µm. The overall amplitudes of sub harmonic whirl motion are similar to those predicted as the rotor accelerates. Note that during rotor acceleration, see Fig. 10 (c), the rotor onset speed of subsynchronous whirl (~19 krpm) is higher than the rotor speed (~12 krpm) at which the subsynchronous whirl disappears during rotor deceleration, i.e., a marked hysteresis is apparent.

Figure 12 presents the RBS synchronous motion versus rotor speed for the fast rotor (de)acceleration cases and imbalance u=20 µm. The synchronous amplitude shows a strong stiffness hardening effect with the peculiar jump phenomenon. The figure includes the predicted linear response, Eq. (7), and the nonlinear (numerical) synchronous responses. Note the typical hysteresis while the rotor decelerates. For details on this nonlinear aspect, please see Ref. [23].

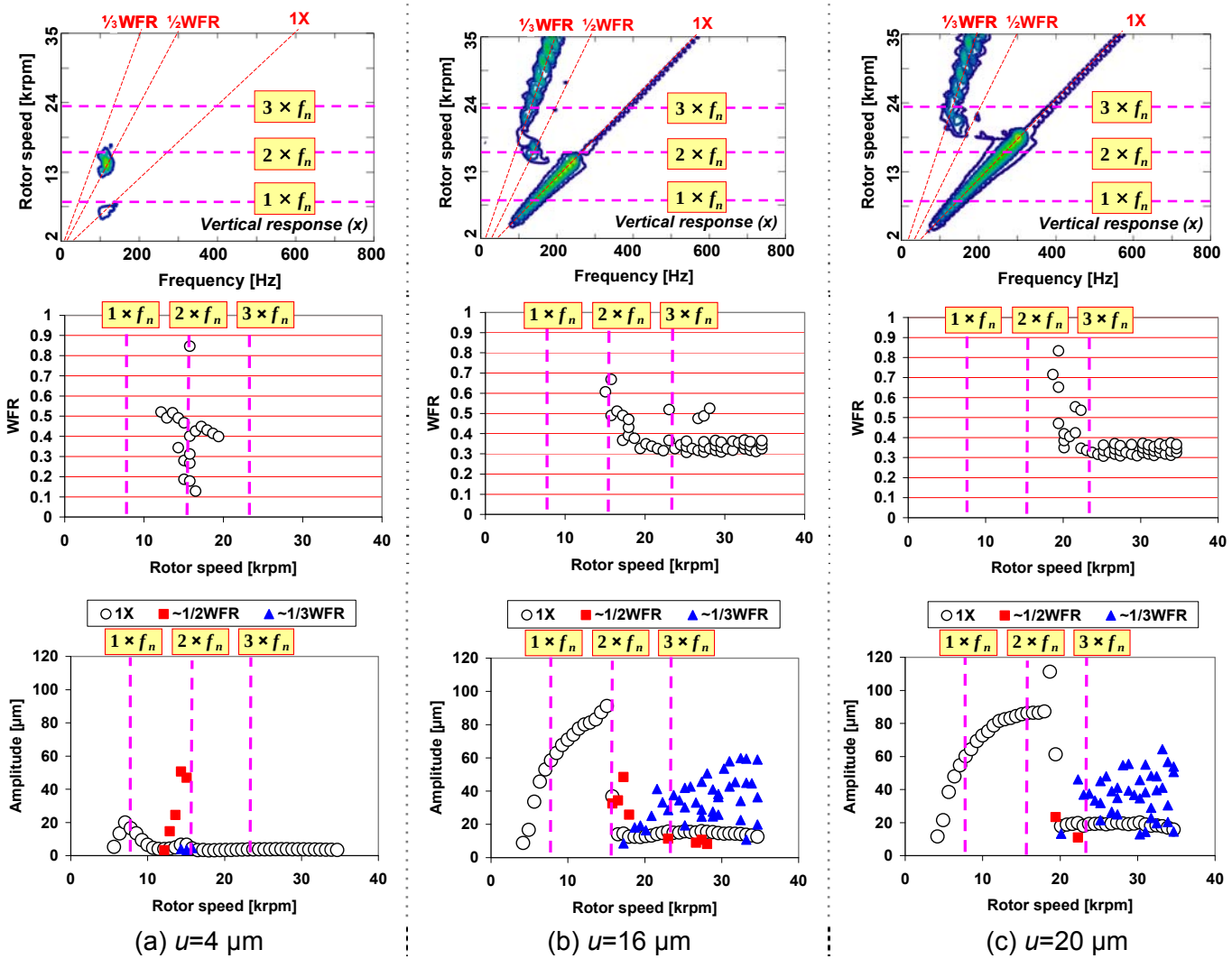

Fig. 10 Effect of imbalance (u) on rotor vertical (x) motion amplitudes. Imbalance u=4 µm, 16 µm and 20 µm (left to right graphs). Rotor accelerates at α=283 Hz/s. (Top) vibration amplitude contour plots, (Middle) whirl frequency ratio, and (Bottom) amplitudes of synchronous and subsynchronous (~½WFR and ~⅓WFR) motions versus rotor speed. FB: γ=0.14.

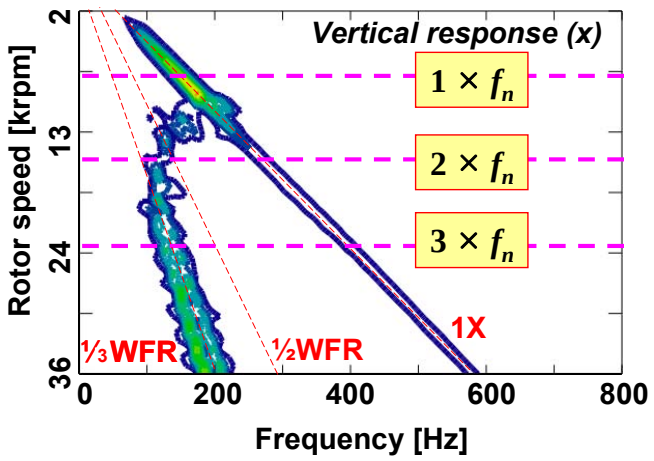

Fig. 11 Vibration amplitude contours: Predicted vertical (*x*) rotor motions while rotor decelerates, *α*=-283 Hz/s. Imbalance *u*=20 μm and FB: *γ*=0.14

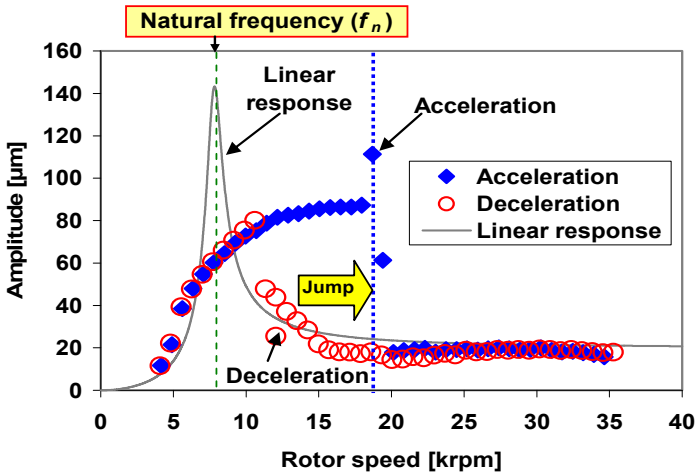

Fig. 12 Amplitudes of rotor synchronous motion during rotor acceleration and deceleration α=+/- 283 Hz/s. Response for linear RBS also shown. Large imbalance *u*=20 μm and FB: *γ*=0.14.

Effect of FB structural loss factor on RBS response

In a FB, the loss factor (γ) is a measure of its mechanical energy dissipation ability. The higher the γ, the more *damping* the foil bearing has. Conventional gas film bearings are notorious for their little viscous type damping; hence the need to have GFBs with reliable (and predictable!) mechanical energy dissipation characteristics.

In the following predictions, the rotor with imbalance u=8 μm accelerates at α=+283 Hz/s. Figure 13 shows the contour plot of vertical rotor motions (x), the whirl frequency ratio (WFR=ω/Ω), and components of synchronous and subsynchronous (~½WFR and ~⅓WFR) motions versus rotor speed. The graphs, left to right, correspond to predicted responses for bearings with increasing material loss factors, γ=0.07, 0.20 and 0.28. See Fig. 7 for predictions with γ=0.14.

As expected, the FB loss factor significantly affects the onset and persistence of the rotor sub harmonic motions. These motions are more noticeable as γ decreases, the lesser the damping in the RBS. For γ>0.2, ⅓WFR frequency components disappear. As γ increases, the peak amplitude of synchronous response decreases dramatically since x_{max}/u~$1/\gamma$. For the bearing with smallest γ=0.07, the synchronous motion evidences the typical stiffness hardening effect and an amplitude jump at ~15 krpm. For γ<0.07, and at a rotor speed equal to ~twice the natural frequency, the ½ WFR motions gradually bifurcate into ⅓ WFR (from 15 krpm to 20 krpm). The 0.33 WFR motions persist from 20 krpm to the top speed (36 krpm). References [21,22,27,28] show test FBs with loss factors (γ) ranging from 0.06 to 0.50, depending on their mechanical complexity (generation type). A viscoelastic layer underneath the top foil also enhances mechanical energy dissipation [29].

During rotor deceleration at -283 Hz/s, Fig. 14 displays the contour plot of vertical (x) rotor motion amplitudes for u=8 μm and γ=0.07. Between rotor acceleration, see Fig. 13 (a), and deceleration cases, notable differences in the frequency component of the rotor response are apparent at rotor speeds ranging from 8 ~ 15 krpm (1×f_n ~ 2× f_n). In this speed regime, ~½WFR motions are apparent during rotor deceleration. On the other hand, as the rotor accelerates, the synchronous whirl motions dominate the rotor response from 8~15 krpm. Overall, the amplitude components of subsynchronous whirl are similar as the ones during rotor acceleration.

For a FB with γ =0.07 and operating with imbalance u=8 μm, Fig. 15 depicts the amplitudes of synchronous response versus rotor speed during rotor acceleration and deceleration. As the rotor accelerates, the hardening nonlinearity is pronounced and showing a distinctive jump (down). On deceleration, the rotor synchronous response appears free of nonlinearities. The rotor speeds at which the amplitudes peak are 14.3 krpm (98 μm) while accelerating, and 7.1 krpm (38 μm) while decelerating. Recall that the linear f_n=130 Hz (7,797 rpm).

CONCLUSIONS

The static load and dynamic forced performance of GFBs depends mainly on the structural properties and geometry of the underspring support. Rotors supported on foil bearings often show at high speed operation peculiar responses with sub harmonic whirl motions of large amplitude. These whirl motion have been at times mistakenly attributed to an instability; hence, apprehension follows as per the widespread usage of foil bearings in commercial rotating machinery.

Earlier work by the first author demonstrated, based on empirical evidence and analysis, that foil bearings are nonlinear structural elements prone to induce forced responses with multiple frequency components (not a classical instability). The sub synchronous motions are not a self-excited rotordynamic instability but a structural nonlinearity exacerbated by mass imbalance, i.e. by an external forcing function.

This paper extends the earlier work to predict (numerically) the response of a simple FB supported rotor and to quantify the effects of rotor acceleration (deceleration) on the onset and persistence of sub harmonic whirl motions, and including hysteresis effects on the jump phenomenon. In addition, predictions also show the effect of increasing mass imbalances on exacerbating the severity of the nonlinear response, and increasing foil bearing loss factors, a measure of their damping ability, on reducing amplitudes of motion and elimination sub synchronous whirl motions.

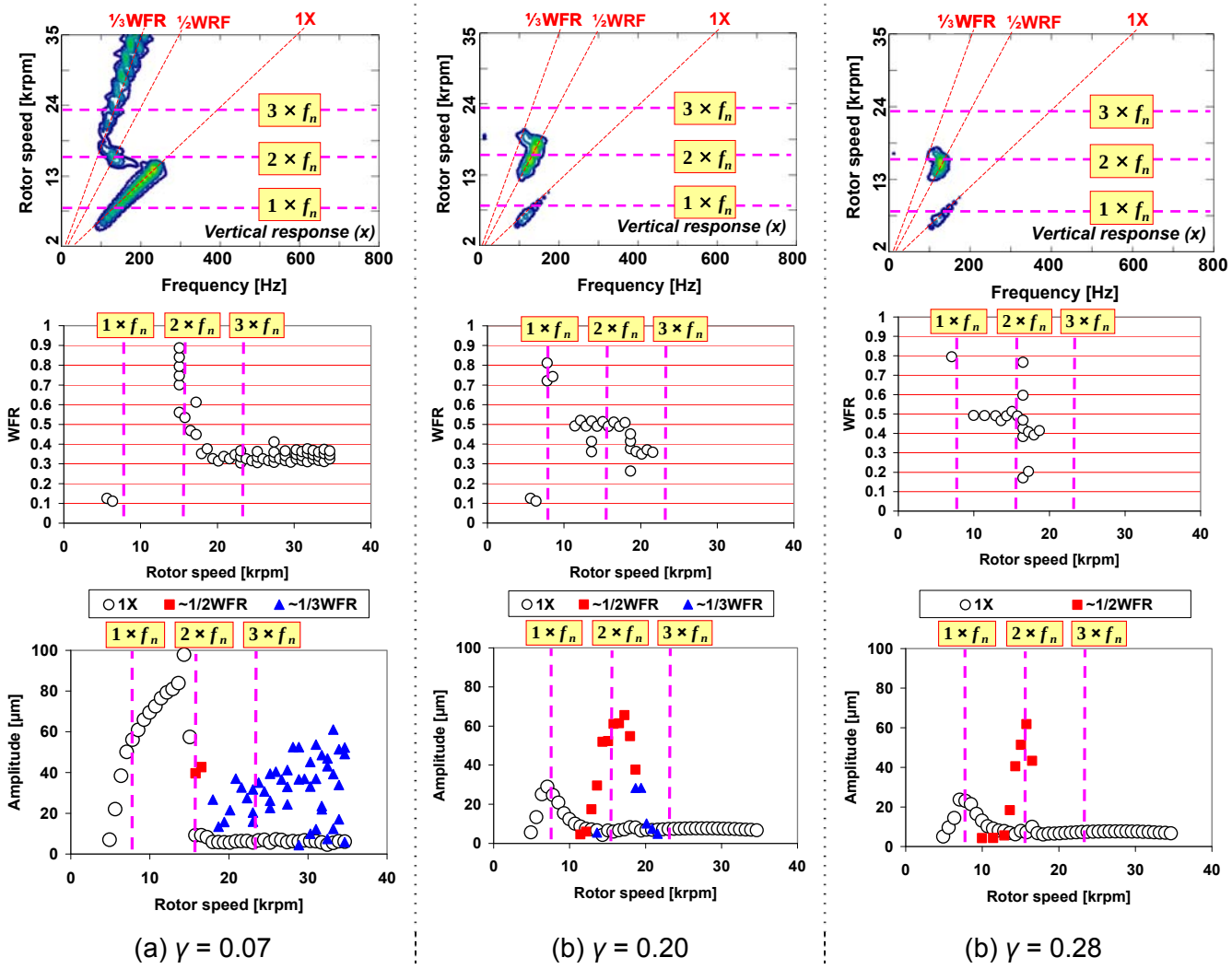

Fig. 13 Effect of FB loss factor (*γ*) on the rotor vertical (*x*) motion amplitudes. Loss factors *γ*=0.07, 0.20 and 0.28 (left to right graphs). Rotor acceleration *α*=283 Hz/s, imbalance *u*=8 μm (Top) vibration amplitude contour plots, (Middle) whirl frequency ratio, and (Bottom) amplitudes of synchronous and subsynchronous (~½WFR and ~⅓WFR) motions versus rotor speed.

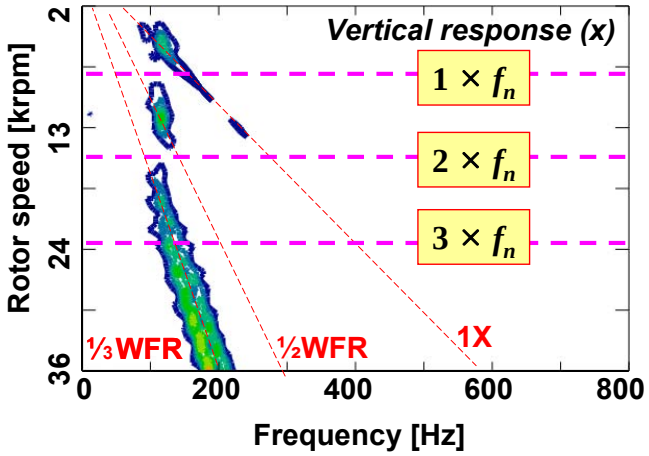

Fig. 14 Vibration amplitude contours: Predicted vertical (*x*) rotor motions while rotor decelerates, *α*=-283 Hz/s. Imbalance *u*=8 μm and FB: *γ*=0.07

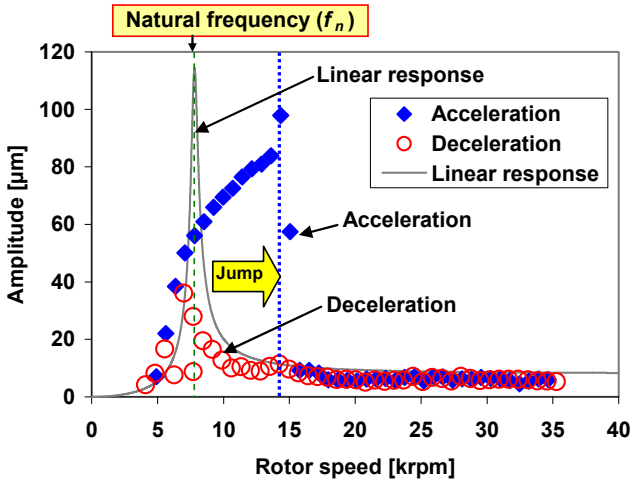

Fig. 15 Amplitudes of rotor synchronous motion during rotor acceleration and deceleration *α*=+/-283 Hz/s. Response for linear RBS also shown. Imbalance *u*=8 μm and FB: *γ*=0.07.

Predicted nonlinear responses display rotor motions with two major whirl frequencies, at 50% (½ WFR) and 33% of rotor speed (⅓WFR) for operation above the system natural frequency. During rotor acceleration, whirl motions at 50% rotor speed appear and track the rotor speed. As the rotor speed further increases, the whirl motions bifurcate into a ⅓WFR. For rotor deceleration from a high speed, well above the system natural frequency, the overall amplitude of the synchronous and subsynchronous rotor responses are smaller than those for rotor acceleration. Lower speed ramp rates lead to more pronounced and abundant sub harmonic whirl motions.

Rotor imbalance awakens and exacerbates the nonlinear response of a rotor-foil bearing system. The predictions show a strong stiffness hardening effect with jump phenomenon and the onset and persistence of whirl motions tracking rotor speed at fixed ratios, first ½ and later 1/3, for example. Larger magnitudes of imbalance produce a stronger hysteresis in rotor response during slow acceleration and deceleration cases. The magnitude of material damping, i.e., loss factor γ, is paramount to prevent and delay the onset of subsynchronous whirl motions with large amplitudes reaching a limit cycle. Bearings with $\gamma <$ 0.07 produce a distinct hysteresis in the synchronous and subsynchronous responses as the rotor accelerates or decelerates, i.e. markedly different responses.

Most RBS implementing bump-type foil bearings are prone to show a forced nonlinearity with subsynchronous whirl frequencies and amplitudes largely affected by rotor imbalance. Elimination of the nonlinear response may not be possible in practice; albeit its persistence, since the GFBs are resilient, seems not to penalize the RBS efficiency although long life operation remains questionable. Improvements in GFB design and materials offer configurations with large material damping to ameliorate subsynchronous rotor motions resulting from the nonlinear effect of the hardening support structure. Fast rotor start up and coast down procedures are recommended to avoid the build up of excessive nonlinear RBS responses; hence reductions in rotor inertia or a larger drive torque become necessary. The results of this paper bring to attention design and operation considerations for the appropriate selection and use of GFBs in commercial applications.

ACKNOWLEDGMENTS

The support of the TAMU Turbomachinery Research Consortium is acknowledged. Parts of the investigation were conducted under NASA NRA on Subsonic Rotary Wing, SSRW2-1.3 Oil-Free Engine Technology (Foil Gas Bearing Modeling). Grant Cooperative Agreement NNX07P98A. The first author thanks undergraduate students Laura Wells and Katherine Janica who wrote versions of the predictive code with the accompanying frequency domain analysis and filtering.

NOMENCLATURE

f_n	RBS natural frequency [Hz]
F_{FBs}	FB structural force, $K_1r+K_2r^2+K_3r^3$ [N]
$K_{1\text{-}3}$	FB structure nonlinear stiffness coefficients
K_{FBs}	$= K_1+2K_2r+3K_3r^2$. Nonlinear FB structural stiffness [N/m]
M	Rotor mass [kg]
r	$=(x^2+y^2)^{1/2}$. Rotor motion amplitude [m]
t	Time [s]
u	Mass imbalance offset [m]
WFR	$= \omega/\Omega$ .Whirl frequency ratio
x,y	Rotor displacements, vertical and horizontal [m]
α	Rotor angular acceleration [rad/s^2]
γ	FB structural loss factor
θ	Rotor angular displacement [rad]
ω	Rotor whirl frequency [rad/s]
Ω	Rotor angular speed [rad/s]

Acronyms

FB	Foil bearing
RBS	Rotor-bearing system

REFERENCES

[1] Bruckner, R. J., 2004, "A Propulsion System Analysis of Oil Free Turbomachinery for Aviation Turbofan Engines," AIAA Paper No. 2004-4189, *Proceedings of 40th AIAA/ASME/SAE/ASEE Joint Propulsion Conference and Exhibit*, Fort Lauderdale, FL, Jul.

[2] DellaCorte, C., Pinkus, O., 2000, "Tribological Limitations in Gas Turbine Engines: A Workshop to Identify the Challenges and Set Future Directions" NASA/TM-2000-210059/REV1, NASA, OH.

[3] Kim, T.H., and L. San Andrés, 2006, "Limits for High Speed Operation of Gas Foil Bearings," ASME J. Tribol., **128**, pp. 670-673

[4] Kim, T.H., and L. San Andrés, 2008, "Heavily Loaded Gas Foil Bearings: a Model Anchored to Test Data," ASME J. Eng. Gas Turbines Power, **130**(1), p. 012504

[5] San Andrés, L., and Kim, T.H., 2009, "Thermohydrodynamic Analysis of Bump Type Gas Foil Bearings: A Model Anchored to Test Data," ASME J. Eng. Gas Turbines Power, **132**(4), p. 042504.

[6] Rubio, D., and San Andrés, L., 2006, "Bump-Type Foil Bearing Structural Stiffness: Experiments and Predictions," ASME J. Eng. Gas Turbines Power, **128**, pp. 653-660.

[7] San Andrés, L., Rubio, D., and Kim, T.H, 2007, "Rotordynamic Performance of a Rotor Supported on Bump Type Foil Gas Bearings: Experiments and Predictions," ASME J. Eng. Gas Turbines Power, **129**, pp. 850–857.

[8] Kim, T. H., and San Andrés, L., 2009, "Effect of Side End Pressurization on the Dynamic Performance of Gas Foil Bearings – A Model Anchored to Test Data," ASME J. Eng. Gas Turbines Power, **131**(1), p. 012501

[9] Kim, T.H., and San Andrés, L., 2009, "Effects of a Mechanical Preload on the Dynamic Force Response of Gas Foil Bearings - Measurements and Model Predictions," STLE Tribol. Trans., **52**, pp. 569-580

[10] Kim, T. H., San Andrés, L., 2010, "Thermohydrodynamic Model Predictions and Performance Measurements of Bump-type Foil Bearing for Oil-Free Turboshaft Engines in Rotorcraft Propulsion Systems," ASME J. Tribol., **132**(1), p. 011701.

[11] Heshmat, H., 1994, "Advancements in the Performance of Aerodynamic Foil Journal Bearings: High Speed and Load Capacity," ASME J. Tribol., **116**, pp. 287-295.
[12] Heshmat, H., 2000, "Operation of Foil Bearing Beyond the Bending Critical Mode," ASME J. Tribol., **122**(1), pp. 192-198.
[13] San Andrés, L. and Kim, T. H., 2008, "Forced Nonlinear Response of Gas Foil Bearing Supported Rotors," Tribol. Int., **41**(8), pp. 704-715.
[14] Noah, S., and Sundararajan, P., 1995, "Significance of Considering Nonlinear Effects in Predicting the Dynamic Behavior of Rotating Machinery," J. Vib. Control, **1**, pp. 431-458.
[15] Yamamoto, T., and Ishida, Y., 2001, *Linear and Nonlinear Rotordynamics: A Modern Treatment with Applications*, Wiley, New York.
[16] Jeng, J-D., Kang, Y., and Chang, Y-P., 2007, "Characteristics in Response Integration and Bifurcation of a Forced Duffing Oscillator," ASME Paper No. GT2007-28118.
[17] Rudloff, L., Arghir, M., Bonneau. O., and Matta, P., 2010, "Experimental Analyses of A First Generation Foil Bearing. Start-up Torque and Dynamic Coefficients," ASME Paper No. GT2010-22966.
[18] Conlon, M., Dadouche, A., Dmochowski, W., Payette, R., ad Bedard, J.-P., 2010, "A Comparison of the Steady-State and Dynamic Performance of First- and Second-Generation Foil Bearings," ASME Paper No. GT2010-23683.
[19] Vistamehr, A., 2009, "Analysis of Automotive Turbocharger Nonlinear Vibrations Including Bifurcations," M.S. Thesis, Texas A&M University, Mechanical Engineering, College Station, TX, December.
[20] Nayfeh, A. H., and Balachandran, B., 1989, "Modal Interactions in Dynamical and Structural Systems," ASME Appl. Mech. Rev., **42**, pp.175-201.
[21] Rubio, D., and San Andrés, L., 2007, "Structural Stiffness, Dry Friction Coefficient, and Equivalent Viscous Damping in a Bump-Type Foil Gas Bearing," ASME J. Eng. Gas Turbines Power, **129**, pp. 494-502.
[22] Kim, T. H., Breedlove, A. W., and San Andrés, L., 2009, "Characterization of a Foil Bearing Structure at Increasing Temperatures: Static Load and Dynamic Force Performance," ASME J. Tribol., **131**(4), p. 041703.
[23] Wang, J. K., and Khonsari, M. M., 2006, "On the Hysteresis Phenomenon Associated with Instability of Rotor-Bearing Systems," ASME J. Tribol., **128**, pp. 188-196.
[24] Ginsberg, J. H., 2001, *Mechanical and Structural Vibrations*, 1st Ed., John Wiley & Sons, Inc., NY, pp. 152-154.
[25] Childs, D., 1993, T*urbomachinery Rotordynamics*, Wiley, New York, pp. 77-81
[26] San Andrés, L., Modern Lubrication Theory Course Notes 5: Dynamics of a Simple Rotor-Fluid Film Bearing System, Open Source: https://repository.tamu.edu/handle/1969.1/93245, accessed Jan. 2011.
[27] San Andrés, L., Ryu, K., and Kim, T.H., 2011, "Identification of Structural Stiffness and Energy Dissipation Parameters in a Second Generation Foil Bearing: Effect of Shaft Temperature," ASME J. Eng. Gas Turbines Power, **133**(3), p. 032501.
[28] San Andrés, L., Camero, J., Muller, S., Chirathadam, T., and Ryu, K., 2010, "Measurements Of Drag Torque, Lift Off Speed, And Structural Parameters In A 1st Generation Floating Gas Foil Bearing," Paper No. WeD-1-5, *Proceedings of 8th IFToMM International Conference on Rotordynamics*, Sep. 12-15, Seoul, Korea.
[29] Lee, Y.B., Kim, T.H., Kim, C.H., Lee, N.S., and Choi, D.H., 2004, "Dynamic Characteristics of A Flexible Rotor System Supported By A Viscoelastic Foil Bearing (VEFB)," Tribol. Int., **37**, pp. 679–687.